Dynamic Manipulation of Friction in Smart Textile Composites of Liquid-Crystal Elastomers

Takuya Ohzono,* Mohand O. Saed, Youfeng Yue, Yasuo Norikane, and Eugene M. Terentjev*

Smart surfaces that reversibly change the interfacial friction coefficients in response to external stimuli enable a wide range of applications, such as grips, seals, brake pads, packaging films, and fabrics. Here, a new concept of such a smart frictional system is reported: a composite film of a plain-weave polyester textile sheet and a thermoresponsive nematic liquid crystalline elastomer (LCE). The composite is deployed with retractable microundulations of the elastomer inside each weave mesh, enabling dramatic changes of the contact interface with the opposing surface on LCE actuation, which is induced, e.g., by a change in temperature (T). At room T, the protruding viscoelastic parts of LCE in the nematic phase make contact with the opposing flat surface, resulting in a very high friction. At an elevated T ($\approx$50 °C, isotropic phase), the undulations of LCE surface are retracted within the thickness of the textile, and the contacts are limited to small regions around overlapping textile fibers, lowering the friction dramatically. This effect is fully reversible on heating/cooling cycles. The surface undulations are spontaneous, i.e., fabricated without any lithographic or alignment techniques. The present composite opens a new way for the application of sheets/films with switchable friction enabled by stimuli-responsive LCEs.

Functional flexible polymer films and sheets[1] such as textiles, tapes, and laminating materials, are used in many applications. Their friction against other surfaces[2–4] is one of the most important factors in their practical use, since this affects the force transmission between objects, e.g., in gripping and sliding, and in tactile sensing. In many situations, the ability to switch their friction characteristics on demand[5–9] would

Dr. T. Ohzono, Dr. Y. Yue, Dr. Y. Norikane
Research Institute for Electronics and Photonics
National Institute of Advanced Industrial Science and Technology (AIST)
1-1-1 Higashi, Tsukuba 305-8565, Japan
E-mail: ohzono-takuya@aist.go.jp
Dr. M. O. Saed, Prof. E. M. Terentjev
Cavendish Laboratory
University of Cambridge
J. J. Thomson Avenue, Cambridge CB3 0HE, UK
E-mail: emt1000@cam.ac.uk

be useful. To design such smart contact surfaces, one or more of the parameters governing the friction should be altered through reversible changes in the material components.[10,11]

The parameters controlling friction can be reviewed by considering a model for the dry friction in polymers and elastomers, which is known as the "adhesive friction model."[2,3,12] In this model, the friction force arises from the shear strength to open the contact interface. Including the energy dissipation effect due to the viscoelastic response, and the applied sliding speed, v, the overall friction force, F, may be written as

$$F = \alpha F_0 \left[1 + \phi(v) \right] \tag{1}$$

where F_0 is the friction per unit area of real contacts at the zero crack opening speed, $\phi(v)$ is a nondimensional factor expressing the velocity-dependent viscoelastic dissipation, and α is the ratio of the real contact area to the apparent one ($0 < \alpha < 1$). F_0 is related to the static interfacial energy of the two materials in contact. The geometric factor α should depend on the applied apparent normal pressure, P (or load L), and usually shows a monotonic increase with P, known as the "Amontons law." Additionally, the variation in the elastic modulus of the materials in contact, which also affects the interfacial deformation, may be incorporated in α. For the case of friction on the rough surface, the local topography effect can also be included in α: the smaller or larger value should be assumed for the corrugated or smooth surface, respectively.

According to Equation (1), there are, in principle, multiple parameters available to tune the friction. If materials in contact are changed, F_0 may change via the altered surface energies; parameters α and $\phi(v)$ also may change via the altered storage and loss moduli, respectively. If the surface topography is modulated, α is directly affected as well. Therefore, surface designs that induce drastic changes of materials in contact and the surface topography, will provide friction with a wide dynamic range.

For this purpose, ideas mainly relying on the surface topography changes have been explored, using mechanical buckling-based surface wrinkles[7–9,13] and fingerprint textures of a chiral nematic polymer coating.[5,6,14] The former system requires the application of macroscopic strain to the sample to generate the microscopic surface wrinkling, which makes it not useful as freestanding sheets. Although the latter liquid crystal polymer systems[15,16] are attractive, the good wrinkling effect requires

specific alignment layers for the polymer on the surface, which is technically challenging and only useful in limited settings. Liquid crystal elastomers (LCEs) are very promising systems to induce very large topographical changes via phase transitions[17–25] that can be triggered by multiple stimuli, such as temperature, light, and chemicals. In addition, the LCEs show drastic changes in the bulk viscoelasticity[18,26–30] which allows to tune friction via the F_0, α, and ϕ entries in the basic Equation (1). However, the development of the dynamic frictional system through the combination of these effects remains an open challenge.

Here, we propose a new composite system, combining a polyester textile and thermally responsive nematic LCEs. The generic idea is to simultaneously change the contact area through the topographic effects that influence the magnitude of α, change materials in direct contact, which affects F_0 and ϕ, and also use the dynamic soft-elasticity of a nematic LCE phase to separately affect ϕ via the enhanced internal dissipation. All of these changes occur on LCE actuation upon an external stimulus, e.g., temperature change that induces the phase transition of incorporated LCEs. Then, Equation (1) is rewritten indicating the relevant variables as

$$F(T,L,v) = \alpha(T,L,v)\,F_0\,(T)\,[1+\phi(T,v)] \qquad (2)$$

The proposed changes become possible through a fine geometrical design of thermally retractable microundulations of LCE "pockets" formed in each opening of the textile mesh. They are also designed to be fabricated through a simple lithography-free deposition method. At room temperature (RT), the buckled viscoelastic LCE parts in the nematic phase protrude out of the composite film and make contact with the opposing surface

over a large area, resulting in high friction. In contrast, at high temperature (HT) that turns the LCE isotropic, the undulations of the elastomer are flattened and retracted within the confines of the textile mesh. As a result, the contacts with the opposing surface are limited to small regions around overlapping points of the hard textile fibers, lowering friction dramatically.

Our system is the composite (**Figure 1**) of a nematic LCE[23,25,30] (Figure S1, Supporting Information) and a plain-weave textile, in which the volume other than the fiber components within the thickness of the textile is almost fully filled with the LCE (Figure 1b), as in the rubber-coated textiles. The basic properties of the present LCE have been characterized using the neat LCE samples, and listed in the Supporting Information: polymerization reactions (Figure S2, Supporting Information), nematic-isotropic transition T_{NI} (Figure S3, Supporting Information), LC phase (Figures S3 and S4, Supporting Information), thermal actuation (Figure S5, Supporting Information), and viscoelastic response (Figure S6, Supporting Information). In brief, the LCE has $T_{NI} \approx 35\ °C$ and the glass transition temperature of $\approx-40\ °C$, spontaneous and reversible changes of the shape with the uniaxial strain of at least 30%, and of the soft viscoelasticity with the high loss factor $\tan\delta$ in the nematic phase.[30]

The fabrication of the composite begins with molding the LCE precursor and the textile sheet between two flat glass slides under normal pressure,[31] and its thermal curing in the isotropic phase (Figure 1a, Methods). The first thiol-ene reaction, creates a random isotropic polymer network. During annealing of the peeled freestanding sample, the solvent is evaporated, causing the volumetric shrinkage. Since the textile lattice is locally rigid, the shrinkage occurs exclusively in the direction
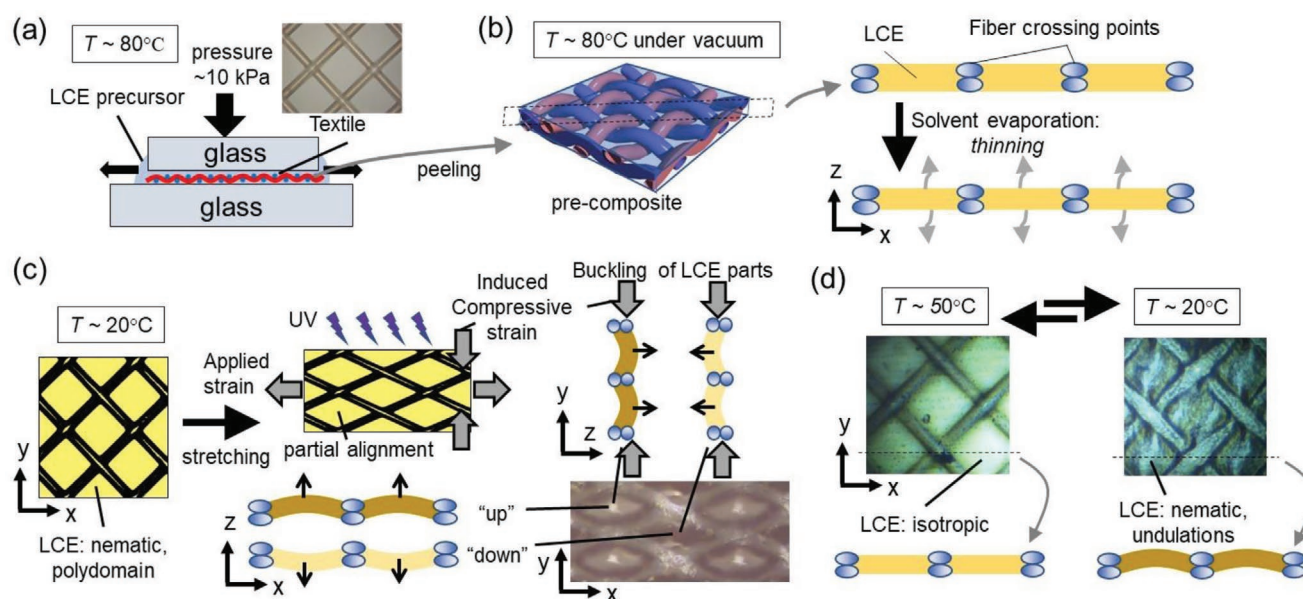

Figure 1. Preparation of the LCE–textile composite sheet with microshape changeability. a) The LCE precursor with the textile between two glass slides undergoes the first cross-linking reaction at elevated temperature (isotropic phase). b) Drying the peeled sample under vacuum, prompting solvent evaporation and volume contraction. c) The second network crosslinking by UV irradiation under local uniaxial strain at RT (nematic phase). The LCE parts buckle protruding in one of the out-of-plane directions, "up" or "down," alternatively along the nearest neighboring mesh openings. This structure is "memorized" by the secondary crosslinking in the nematic phase. d) Release of applied tensile strain and annealing in isotropic phase causes restoring of the original shape, memorized in the isotropic state of LCE and the original textile shape with the square mesh opening. After cooling back to RT, the further modulated undulations of LCE segments appear due to the mismatch between the square shape of the mesh and the secondary memorized shape.

normal to the sample plane (Figure 1b), which is different from the neat LCE systems without constraints of the textile frame.

Then, the sample is uniaxially stretched at RT (in the nematic state) to the strain of 30% in the diagonal direction of the square mesh openings (Figure S7, Supporting Information), which is the most compliant direction (x) of the plain-weave textile. Under this strain, the LCE parts at mesh openings adopt a buckled surface structure in response to the induced local compressive strain (Figure S8, Supporting Information) of $\approx-45\%$ in the orthogonal direction (y) (Figure 1c; Figure S9a, Supporting Information).

Two energetically equal states of buckling appear: bending "up" or "down," which is confirmed by the observation of both sides at the same location (Figure S9b,c, Supporting Information). In most parts on the sample, the buckling directions show a regular square pattern, with the nearest neighboring mesh openings shown one opposite to each other. Since the LCE is continuous across neighboring meshes, the alternation of the buckling direction may minimize the bending energy of LCE parts between the mesh openings. In addition to this structural change, the complicated alignment of the nematic director in this buckled state should emerge. This state of the nematic director alignment coupled to the shape is then memorized by the UV-induced second polymerization process that stabilizes the nematic phase.

After the second photo-crosslinking, the applied strain is released and the sample is annealed to equilibrate in a load-free state (Figure 1d). At HT, the original memorized state of the isotropic LCE is restored, and the original textile shape with square mesh opening is also recovered. After cooling back to RT, the modulated undulations of LCE segments, reflecting those formed under the applied strain, appear without changing the square shapes of the mesh. Owing to the mismatch between the naturally square shape of the mesh openings, and the rhombic shape recorded in the nematic phase, additional buckling of the elastomer surface occurs in response to the emerging compressive strain in the x direction. The results also indicate that the additional buckling has lower energy than the simple elongation of LCE parts together with mesh shape deformation without undulation of LCE parts. Since the initial undulations can assist in nucleating the additional buckling, the initial buckling directions memorized under applied strain are retained in the structure (Figure S9a,b, Supporting Information). Upon heating again to $T > T_{NI}$, the undulations retract, restoring the state of the first crosslinked network. Consequently, the temperature change mainly induces reversible alternation of microundulations, while the macroscopic shape of the composite sheet remains approximately constant (Figure S10, Supporting Information).

Since buckling of the LCE segments is the key phenomenon behind the microundulations, the effective aspect ratio, (lateral length)/(thickness), of the LCE segments in the mesh openings is an important parameter (Figure S11, Supporting Information), which depends on the mesh size. In the subsequent study, the composites of the textile with the mesh opening of 0.199 mm (T100) are used as the representative system with ideal microundulations.

The detailed temperature-dependent surface topographies are shown in **Figure 2** (with details in Figures S12 and S13 in the Supporting Information). The undulations of the LCE
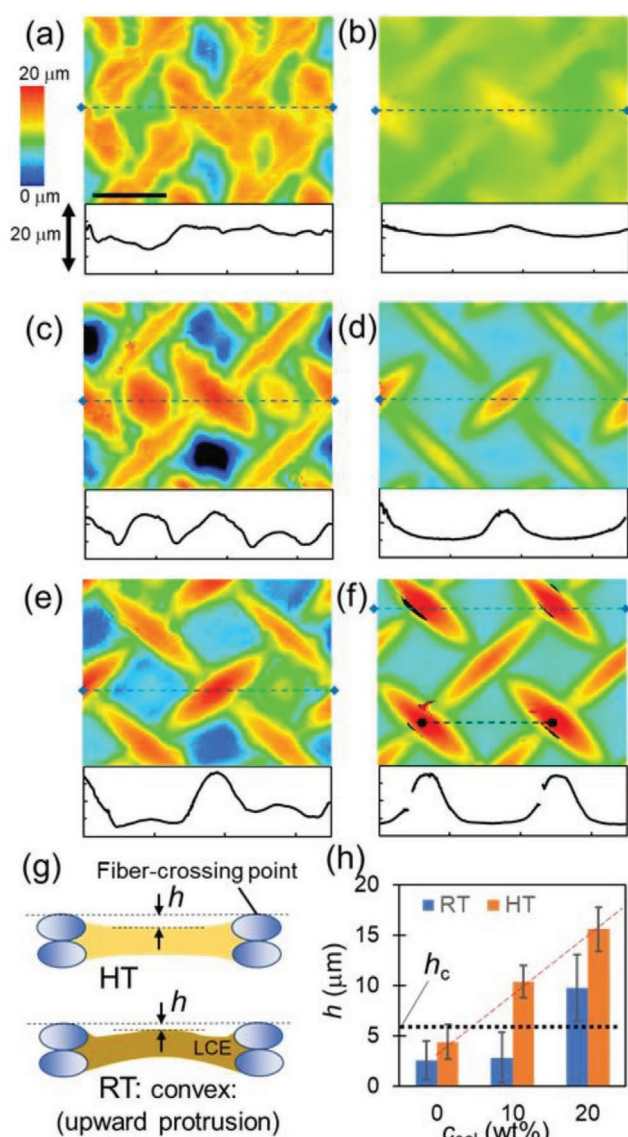

Figure 2. Phase-dependent topography: height images with line profiles along blue dashed lines in the images. Typical images of samples prepared with 0, 10, and 20 wt% of the initial solvent are shown in (a) and (b), (c) and (d), and (e) and (f) panels, respectively. The measurements are at RT (nematic) a,c,e) and at HT (isotropic) b,d,f). Scale bar: 0.2 mm. g) Definition of h, which is the height from the center of the mesh opening (LCE part) to the fiber-crossing point. The schematic is the cross section between the nearest neighboring fiber-crossing points indicated as dashed line in (f). For data at RT, the convex LCE parts were measured. h) Plots of solvent concentration, c_{sol}, and averaged values of h obtained from images with the larger area (Figure S10, Supporting Information) at multiple locations ($N > 10$). The characteristic height value, $h_c \approx 6$ mm, dividing the two contact regimes described later, is shown as a guidance.

parts in the mesh openings at RT (nematic) are retracted at HT (isotropic) (Figure S14, Supporting Information) toward the mid-plane of the sample sheet, and flattened. This is also traced by the diffusion of laser light transmitted through the sample[32] showing the broadening of the diffusion peaks due to the roughening of the interface at RT (Figure S15, Supporting Information).

The amount of the solvent during the preparation, c_{sol}, affects the surface topography via the final thickness of the LCE layer. In particular, it controls the height difference h between the fiber-crossing points and the LCE parts (Figure 2g,h). At HT, h linearly increases at ≈0.5 µm wt%⁻¹ as shown by the red dashed line in Figure 2h. Since the textile half thickness is ≈50 µm, the result indicates that the shrinkage of LCEs near the center of the mesh opening occurs mainly in the direction perpendicular to the film. The nonzero value of h at $c_{sol} = 0$ wt% would be due to the non-negligible curing shrinkage (syneresis)[33] of ≈10% during the present polymerization. At RT, values of h become smaller due to the microundulations of the LCEs. The transformation between two states was fully repeatable over at least ten cycles (Figure S13 and Movie S1, Supporting Information), as expected from the neat sample (Figure S5, Supporting Information) and the other nematic LCEs.[17–25]

The static, F_S, and kinetic friction forces, F_K, between the LCE–textile composite and the flat glass surface were investigated (**Figure 3**a) at the range of load $L < 1$ N, for which the deformation of the polyester fiber at the overlapping point is negligible (Figure S16, Supporting Information). The typical time-dependent frictional signals are shown in Figure 3b, in which F_S and F_K are defined. The temperature-dependent static and kinetic friction coefficients, μ_S and μ_K (Figure 3c,d), are obtained as slopes of the linearly fitted line to the load-dependent friction force. They are roughly classified as either the higher ($\mu_S > 1$, $\mu_K > 0.6$) or lower ranges ($\mu_S < 0.4$, $\mu_K < 0.2$). According to the observation of contact regions (Figure S18, Supporting Information), the high friction corresponds to the states with the larger contact area consisting of LCE parts (leading to a larger α) (Figure S18b–d, Supporting

Information). In the low friction case, contacts only occur at points of overlapping fibers, with small area (Figure S18e–g, Supporting Information). In particular, the sample prepared with 10 wt% solvent shows maximum T-dependent changes in both μ_S and μ_K, each of which shows almost sixfold increase on cooling from HT to RT. For comparison, the best results on the increase of friction in a LC polymer layer were at most twofold,[6,14] and only when two patterned surfaces were against each other. In the deformation-induced wrinkled bilayer surface[7,8] the friction increase was at most 1.5-fold, see the review[13] for detail. The results demonstrate the effectiveness of the present composite design with T-dependent topographical changes on the dynamic friction.

Now let us briefly discuss the observed difference between F_S and F_K illustrated in **Figure 4**, as functions of the normal load, and the sliding speed. In general, F_S at $L = 0$ is of the same order of magnitude as the adhesive strength, σ_{ad}. Since σ_{ad} between the glass surface and the LCE at RT after the dwell time of ≈30 s is in the order of 0.1 MPa,[30] F_S at $L = 0$ with the apparent area of interface ($A = 133$ mm²) can be estimated as $\alpha A \sigma_{ad} \approx 1$ N, where $\alpha \approx 0.1$ is the typical ratio of the contact area at $L = 0$ to A. This corresponds roughly to the nonzero values of the fitted line on the experiments at RT on 0 and 10 wt% solvent systems at $L = 0$, giving ≈0.9 N (Figure S17a, Supporting Information) and ≈0.4 N (Figure 4a), respectively. The effect becomes smaller for the kinetic frictions (Figure 4b), which show lines through the origin at $L = 0$, because of the interfacial sliding; no dwell time for the contact area growth.

Both F_S and F_K also increase with the sliding velocity v (Figure 4c,d) while at constant load L. The difference is most
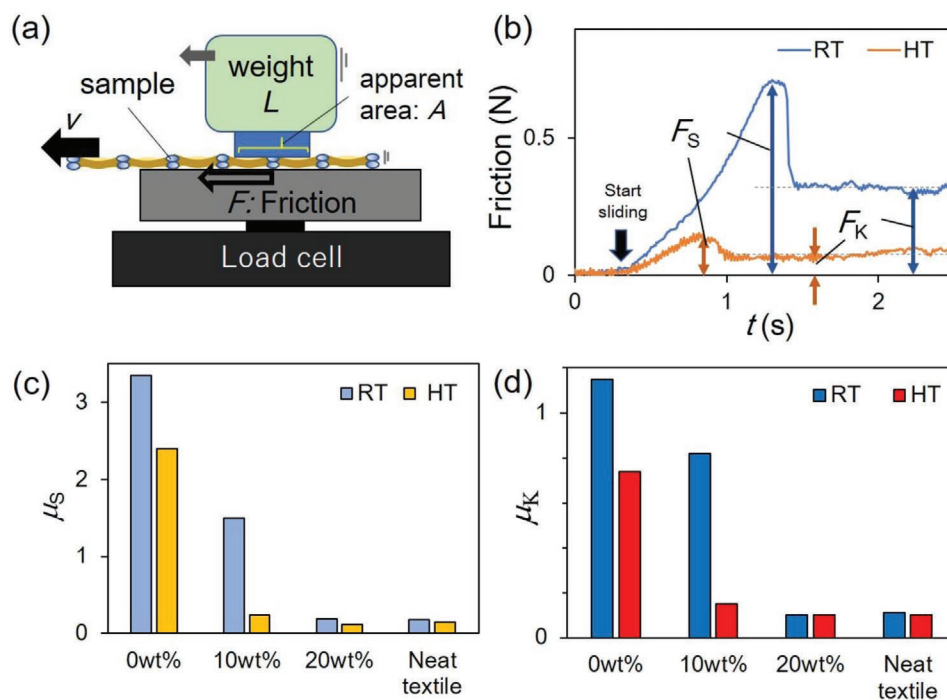

Figure 3. Friction tests. a) Schematic for friction tests. b) Example of the friction signal and the definition of static and kinetic frictions, F_S and F_K, respectively. The data on the sample prepared with 10 wt% solvent at $v = 5$ mm s⁻¹ with $L = 0.3$ N (apparent normal pressure of 2.2 kPa) are shown. c) Static, μ_S, and d) kinetic, μ_K, friction coefficients, obtained as slopes of plots of friction force versus normal load.

**ADVANCED
SCIENCE NEWS**
www.advancedsciencenews.com

**ADVANCED
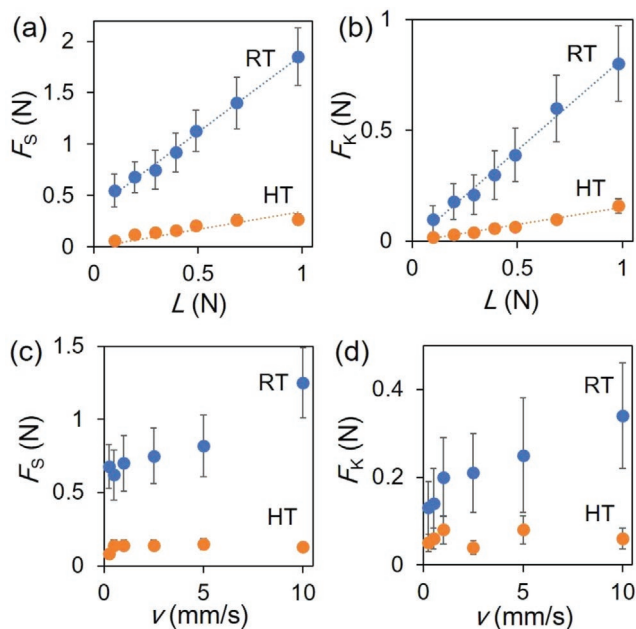MATERIALS
INTERFACES**
www.advmatinterfaces.de

Figure 4. Plots of friction on composite prepared with solvent at 10 wt%. Plots of a) F_S and b) F_K versus normal load L at RT and HT ($v = 2.5$ mm s). Plots of c) F_S and d) F_K versus sliding speed v at RT and HT ($L = 0.3$ N).

striking at RT. The majority of the frictional interface is assumed to be the viscoelastic nematic LCE surface, with $\tan\delta$ of ≈0.7 or above (Figure S6, Supporting Information), which should boost viscous dissipation, ϕ, in Equation (2). In contrast, in the isotropic phase at HT, the contact area is greatly reduced. Moreover, the LCE in contact is in the isotropic phase with the lower $\tan\delta \approx 0.3$ or below, and the hard polyester surface at the fiber-crossing points are in contact, which supports most of the load. Note that at RT the friction of the sample prepared with 10 wt% solvent is only slightly larger than that observed on the neat textile (Figure 3c,d). Thus the slight difference would originate from the modest contact with the isotropic LCE parts around the fiber-crossing points (Figure S18e, Supporting Information). Overall, the present dynamic friction is qualitatively explained by T-dependent changes in α and ϕ in Equation (2), which are related to the contact area and viscoelastic property, respectively.

In general, the friction depends on the properties of two surfaces in contact. The present temperature-induced drastic change in friction may be limited to the cases, in which the hard materials with a flat surface are sliding. If, for example, soft materials with surface roughness comparable to the present mesh periodicity are used as the counter surface, the larger contact may be possible even at HT on the sample prepared with 10 wt% solvent, and thus, resulting in the reduction of the dynamic range of the friction. The easy way to optimize the system is to increase the value of h (Figure 2h), according to the deformability and roughness of the counter surface. In addition, the size of the mesh opening and the fiber diameter (Figure S11, Supporting Information), which also should affect h, can be tuned for this purpose. Fatal wear should also be minimized. First, the fundamental wear resistance of the material components, especially, of viscoelastic soft LCEs should be

improved. Additionally, the good adhesion between LCEs and textile fibers may be required. Future work toward practical applications would focus on these issues with the help of the matured technologies known to ordinary rubbers and their composites with textiles and fibers.[34]

In summary, here we report the design of LCE–textile composites with thermally retractable microundulations for the dynamic manipulation of friction coefficients via modulation of the contact states. The buckling-based spontaneous undulations of LCE parts in the openings of the textile mesh develop through a simple lithography-free procedure. The T-dependent interfacial contact states of the LCE–textile composites to a flat glass surface can be tuned by controlling the fine structure. With the optimized design, the LCE–textile composite makes contact at undulated viscoelastic LCE parts in the nematic phase at RT. In contrast, at HT, textile fibers at their crossing points mainly constitute the contacts with the small area. This alternation, which includes the changes in the contact area and replacement of the materials in contact, can modulate friction forces by sixfold. Owing to the simple fabrication of the transformable microstructure, and the possibility of the further optimization, including the fine structural modifications and tuning of LCE properties, the present design could provide a route to smart LCE–textile composite sheets and films that can reversibly change friction on demand. Since the textile[34] provides the LCE with a better mechanical strength, while retaining the flexibility of a freestanding film, the present composite would also be promising for handling and further processing in a wide range of applications, e.g., robot hands, touch screen devises, and smart textiles.

Experimental Section

Materials and Preparation of LCE–Textile Composite: For the preparation of LCE, the methods reported previously were followed,[25,30,35,36] with two steps of crosslinking reactions: a thiol-acrylate Michael addition and a photoinduced radical polymerization of diacrylates, with slight modifications. The diacrylate monomer, 1,4-bis-[4-(6-acryloyloxyhexyloxy) benzoyloxy]-2-methylbenzene (RM82), was purchased from Wilshire Technologies (Figure S1, Supporting Information). The diacrylate spacer, tri(propylene glycol) diacrylate (TPGDA), and two thiol monomers: 2,2′-(ethylenedioxy) diethanethiol (EDDET) and pentaerythritol tetrakis (3-mercaptopropionate) (PETMP), were purchased from Sigma Aldrich. Triethylamine (TEA, Sigma Aldrich) was used as the catalyst of the Michael-addition thiol-ene reaction. Irgacure2959 from BASF was used as the photoinitiator for the radial polymerization of acrylates. As the radical scavenger, butylated hydroxytoluene (BHT, from Sigma Aldrich) was used to suppress the unwanted reaction before UV light irradiation. Toluene (Sigma Aldrich) was used as the solvent. All chemicals were used in their as-received condition with no purification. Three plain-weave polyester (polyethylene terephthalate) textiles composed of a fiber with the diameter of 0.055 mm and different mesh openings (0.368 mm (T60), 0.199 mm (T100), and 0.086 mm (T180)) were purchased from Yamani inc. Japan.

At the specific molar ratio of functional groups shown in Figure S1 (Supporting Information), RM82, TPGDA, EDDET and PETMP were weighed, Irgacure2959 was added at 0.2 wt%, BHT was added at 0.5 wt%, and toluene was added at 0, 10, and 20 wt%. By increasing the amount of TPGDA, it was possible to lower T_{NI} and here it was adjusted to make $T_{NI} \approx 35$ °C. Note that the amount of the solvent was important to control the final thickness of LCE at the mesh openings, and thus varied here to study the effect. After the mixture was gently mixed at an

elevated $T \approx 70\ °C$ for ≈ 10 min, TEA was added at 1.5 wt% to start the Michael-addition reaction between thiol and acrylate groups. The mixture was kept between two glass slides with a textile mesh with thickness of ≈ 0.1 mm at 70 °C (isotropic phase) overnight under a pressure of ≈ 10 kPa applied to the direction normal to the glass surface to squeeze out the excess liquid.[31] The sample was released from the glass mold, and placed at 80 °C in vacuum to remove the solvent. The sample was then cooled down to RT and UV light (365 nm) was applied for 20 min under a uniaxial tensile strain to finalize the crosslinking between the rest of the acrylates. The tensile strain of 30% was applied in the direction of 45° from the yarn direction; each mesh of the textile was thus elongated to a rhombic shape. The locally deformed and aligned state of the LCE segments were memorized at this crosslinking step. Upon releasing the strain, microundulations of the LCE segments were finally formed. For WAXS and mechanical measurements, samples without the mesh were also prepared, and UV light was applied under uniaxial tensile strain of 50% as reference. The samples were annealed at 80 °C in vacuum oven for 12 h before further characterizations.

Characterization of Surface Topography: The temperature-dependent surface topography was observed using the confocal laser reflection microscope (VK-9710, Keyence) with the temperature-controlled plate (Thermo Plate, Tokai-Hit).

Observation of Contact States: The contact state was observed using inverted optical microscope (GX41, Olympus). The sample placed on a cover glass was set on the transparent hot plate (Thermo Plate, Tokai-Hit). From the top side of the sample, a flat glass surface (area of 133 mm^2) with a weight of 30 g (apparent pressure ≈ 2.2 kPa) was gently placed. The contact regions, which appeared darker in most cases due to the change in the refractive index at the interface, were analyzed from the image.

Friction Tests: The friction was evaluated under constant load and sliding speed using a setup, which was similar to the international-standard test method, ISO 8295 (Plastics: Film and sheeting: Determination of the coefficients of friction). First, the sample was placed on a glass surface connected to a load cell (Tribogear Type33, Heidon). A weight (10–100 g) with a flat glass surface (area of $A = 133$ mm^2) was gently placed to apply constant normal load. After a dwell time of 30 s, during which the present LCE relaxed most of the strain,[30] the sample with the weight was pulled (at a constant speed of v of 0.25–10 mm s^{-1}) to start sliding between the sample surface and the bottom glass surface (Figure 3a). The tests were done at $\approx 20\ °C$ (RT) and $\approx 50\ °C$ (HT) under the constant temperature control. The lateral force read by the load cell was measured as the time-dependent friction force. The static friction was defined as the peak value before the actual sliding at the interface of interest. The kinetic friction was obtained by averaging values during steady sliding over several seconds.

Dynamic Scanning Calorimetry (DSC): For differential scanning calorimetry (DSC, DSC4000 PerkinElmer), samples with ≈ 10 mg were loaded into standard aluminum DSC pans. The samples were heated to 90 °C at 10 °C min^{-1}, held isothermally for 5 min, and cooled to $-60\ °C$ at 5 °C min^{-1} to acquire the data. T_{NI} can be found at local minimum of the endothermic peak. The sample was run three times.

Dynamic Mechanical Analysis (DMA): The dynamic mechanical tests of neat LCE samples were performed on a Viscoanalyser-4000, Metravib, in the tension mode, with samples of 0.8 mm film thickness. A rectangular sample (effective length of 10 mm and width of 8 mm) was used. The simple strain of 0.5% was applied at frequencies of 5 and 50 Hz. Data were acquired on cooling at the rate of 3 °C min^{-1} from 80 to $-80\ °C$.

Stress–Strain Curves: The stress–strain curves for the textiles, LCE–textile composites, and neat LCE films on the tensile mode were obtained using a commercial instrument (Tensilon EZ-LX, SHIMAZU). The sample width, thickness, and effective length were 5, 0.09, and 30–50 mm, respectively. The uniaxial tensile stress–strain property in 45° from the axial direction of yarns, which is the softest direction, were evaluated. Separately, the curves in the uniaxial strain in 0° from the axial direction of yarns were obtain with T60 textile (a low-density mesh). The strain rate of extension was 0.06–0.1% s^{-1}. Each measurement was run three times.

Wide-Angle X-Ray Scattering (WAXS): The phase of the present LCE at RT was characterized using a Philips diffractometer using a Philips Copper target (PW-2233/20) with the wavelength of 0.154 nm. The distance between the sample and the imaging area was 100 mm.

Fourier Transform Infrared Spectroscopy (FTIR): The FTIR measurements were performed using a Nicolet iS10 FTIR spectrometer, Thermo scientific. The peaks of thiols and acrylate at 2573 and 811 cm^{-1}, respectively, were evaluated. Samples were prepared and mounted between KBr plates. The initial state was a sample without TEA. The sample placed under 70 °C oven for 24 h after addition of TEA was also prepared. After taking the spectrum, UV light was irradiated for 20 min for evaluation of the final state. The conversion ratios at the end of each reaction were defined as $\xi = \frac{\sigma_{final} - \sigma_{initial}}{\sigma_{initial}}$, where $\sigma_{initial}$ and σ_{final} are the initial and final peak area of each functional group, thiol, or acrylate.

Supporting Information

Supporting Information is available from the Wiley Online Library or from the author.

Conflict of Interest

The authors declare no conflict of interest.

[1] S. Schneegass, O. Amft, *Smart Textiles Fundamentals, Design, and Interaction*, Springer, Cham, Switzerland **2017**.

[2] D. F. Moore, *The Friction and Lubrication of Elastomers*, Pergamon, Oxford **1972**.

[3] B. N. J. Persson, *Sliding Friction Physical Principles and Applications*, Springer, Heidelberg **2000**.

[4] V. L. Popov, *Contact Mechanics and Friction Physical Principles and Applications*, Springer, Heidelberg **2010**.

[5] D. Liu, D. J. Broer, *Soft Matter* **2014**, *10*, 7952.

[6] D. Liu, D. J. Broer, *Angew. Chem.* **2014**, *126*, 4630.

[7] K. Suzuki, Y. Hirai, T. Ohzono, *ACS Appl. Mater. Interfaces* **2014**, *6*, 10121.

[8] K. Suzuki, Y. Hirai, M. Shimomura, T. Ohzono, *Tribol. Lett.* **2015**, *60*, 2.

[9] K. Suzuki, T. Ohzono, *Soft Matter* **2016**, *12*, 6176.

[10] J. Hu, H. Meng, G. Li, S. I. Ibekwe, *Smart Mater. Struct.* **2012**, *21*, 053001.

[11] M. Wei, Y. Gao, X. Li, M. J. Serpe, *Polym. Chem.* **2017**, *8*, 127.

[12] K. Grosch, *Nature* **1963**, *197*, 858.

[13] N. Hu, R. Burgueño, *Smart Mater. Struct.* **2015**, *24*, 063001.

[14] D. Liu, D. J. Broer, *Langmuir* **2014**, *30*, 13499.

[15] Y. Yu, M. Nakano, T. Ikeda, *Nature* **2003**, *425*, 145.

[16] Y. Yue, Y. Norikane, R. Azumi, E. Koyama, *Nat. Commun.* **2018**, *9*, 3234.

[17] J. Küpfer, H. Finkelmann, *Makromol. Chem., Rapid Commun.* **1991**, *12*, 717.

[18] E. M. Warner, M. Terentjev, *Liquid Crystal Elastomers*, Oxford University Press, Oxford **2007**.

[19] A. Sanchez, H. Finkelmann, *Solid State Sci.* **2010**, *12*, 1849.

[20] T. J. White, D. J. Broer, *Nat. Mater.* **2015**, *14*, 1087.

[21] V. P. Tondiglia, T. J. White, *Science* **2015**, *347*, 982.

[22] A. D. Auguste, J. W. Ward, J. O. Hardin, B. A. Kowalski, T. C. Guin, J. D. Berrigan, T. J. White, *Adv. Mater.* **2018**, *30*, 1802438.

[23] M. O. Saed, C. P. Ambulo, H. Kim, R. De, V. Raval, K. Searles, D. A. Siddiqui, J. M. O. Cue, M. C. Stefan, M. R. Shankar, T. H. Ware, *Adv. Funct. Mater.* **2019**, *29*, 1806412.

[24] M. Barnes, R. Verduzco, *Soft Matter* **2018**, *15*, 870.

[25] C. M. Yakacki, M. Saed, D. P. Nair, T. Gong, S. M. Reed, C. N. Bowman, *RSC Adv.* **2015**, *5*, 18997.

[26] S. M. Clarke, A. R. Tajbakhsh, E. M. Terentjev, C. Remillat, G. R. Tomlinson, J. R. House, *J. Appl. Phys.* **2001**, *89*, 6530.

[27] E. M. Terentjev, A. Hotta, S. M. Clarke, M. Warner, G. Marrucci, J. M. Seddon, H. S. Sellers, *Philos. Trans. R. Soc., A* **2003**, *361*, 653.

[28] S. M. Clarke, A. R. Tajbakhsh, E. M. Terentjev, M. Warner, *Phys. Rev. Lett.* **2001**, *86*, 4044.

[29] D. R. Merkel, R. K. Shaha, C. M. Yakacki, C. P. Frick, *Polymer* **2019**, *166*, 148.

[30] T. Ohzono, M. O. Saed, E. M. Terentjev, *Adv. Mater.* **2019**, *31*, 1902642.

[31] T. Ohzono, K. Teraoka, *R. Soc. Open Sci.* **2018**, *5*, 181169.

[32] T. Ohzono, K. Suzuki, T. Yamaguchi, N. Fukuda, *Adv. Opt. Mater.* **2013**, *1*, 374.

[33] S. Zhiquan, *J. Mater. Chem. C* **2018**, *6*, 11561.

[34] D. Rosato, D. Rosato, *Reinforced Plastics Handbook*, Elsevier Science, Oxford **2004**.

[35] D. P. Nair, N. B. Cramer, J. C. Gaipa, M. K. McBride, E. M. Matherly, R. R. McLeod, R. Shandas, C. N. Bowman, *Adv. Funct. Mater.* **2012**, *22*, 1502.

[36] M. O. Saed, R. H. Volpe, N. A. Traugutt, R. Visvanathan, N. A. Clark, C. M. Yakacki, *Soft Matter* **2017**, *13*, 7537.

1901996 (7 of 7)